The Quadrupole as a Source of Energetic Particles: III. Outer Radiation Belt and MeV electrons

R. B. Sheldon [a,*]

[a] *National Space Science & Technology Center, 320 Sparkman Dr, Huntsville, AL 35805*

Jiasheng Chen and T. A. Fritz [b]

[b] *Boston University, 725 Commonwealth Av, Boston, MA*

Abstract

The observation that high speed solar wind streams are correlated with outer radiation belt electrons requires a transducer to convert this mechanical energy to hot electrons. We hypothesize that the high latitude cusp is the ideal location for this acceleration region. We support this hypothesis with two arguments: a forward model to show that that the cusp can theoretically accelerate electrons to MeV energies which then are transported to the radiation belts; and, a backward model that deduces a cusp source based on empirical properties of the radiation belt MeV electrons. Accordingly, in the first half we apply the trapping properties of the static equinoctal cusp to deduce the dynamical response of interplanetary transients; in the second half we analyze several peculiar statistics of MeV electron correlations with solar wind as the response of a non-linear, multi-parameter dependence on the solar wind driver. Our model would permit the formulation of more physically accurate MeV electron predictors, which we demonstrate by connecting physical explanations to several empirical predictors recently published.

Key words: MeV electrons, outer radiation belt, cusp acceleration, high speed solar wind

* Correspondance to:
Email address: `Rob.Sheldon-1@nasa.gov` (R. B. Sheldon).
URL: `rbsp.info/rbs/RbS` (R. B. Sheldon).

1 Introduction

In earlier papers, Sheldon et al. (2005, 2006) (SCF1,SCF2), we argued that a quadrupole trap could function as an accelerator, a cross between a dipole- and Fermi-accelerator, possessing the best features of both. In SCF2 we presented in more detail the way this physical mechanism may explain the somewhat mysterious origin of outer radiation belt MeV electron (ORBE) injections (McIlwain, 1996), and physically link them to solar wind conditions that impact the quadrupole cusp. This placement of source of ORBE outside the dipole but inside the magnetosphere may account for the relatively recent POLAR (Sheldon et al., 1998; Chen et al., 1997, 1998) discovery despite a 40-year search (McIlwain, 1996). Likewise, the physical mechanism we propose may also explain some of the peculiar correlations and non-linear relations observed between ORBE injections and solar wind/magnetospheric activity (Paulikas and Blake, 1979; Baker et al., 1986; Koons and Gorney, 1991; Li et al., 2001b).

Since electrons are ubiquitous, determining whether cusp electrons are locally accelerated or merely transported to the cusp is problematic. We argue for local acceleration two ways: the ions are locally accelerated; and, the electron gradients support transport out of, not into the cusp. In response to those who insist that the trapped energetic ions in the cusp are transported (Chang, 1998; Chang et al., 2001), we argue for a local acceleration (Chen and Fritz, 1998, 2000, 2001a,b; Chen et al., 2001; Chen and Fritz, 2002; Chen et al., 2005a), which suggests that electrons would also be locally accelerated. For those who think the cusp is filled from the ORBE, we demonstrate (Sheldon et al., 1998) that the electron phase space density in the cusp exceeds that of regions on both sides indicating no ready access by transport. But should electrons be transported adiabatically to the ORBE (described below) they exceed the ORBE phase space density, indicating that adiabatic or diffusive transport from the ORBE cannot account for this cusp population, though the converse may still be true. Of course, electrons could conceivably be transported non-adiabatically, but since that would invoke processes indistinguishable from local acceleration, we lump them together.

We also give theoretical support for local acceleration in SCF1, since a trap is thermodynamically preferred for acceleration both because the efficiency of energy conversion is higher for a multi-step, stochastic process, and because the total energy required for particle acceleration is minimized. In table 4 rows 1-9 are explained in detail in SCF1, and we use order-of-magnitude calculations to make two more estimates of the probability of filling the ORBE trap in 2 days with each mechanism: (10) a simple ratio of injection time needed (2 days) divided by the acceleration time (9c); and, (11) the product of (10) times (9d) the ratio of power needed to power available, where power needed is the total

ORBE energy divided by 2 days. Calculation (10) suggests that bowshock Fermi is slightly more likely to inject because the rapidity of acceleration, but the available power is relatively low compared to the cusp, so that factoring in the power requirement, (11), favors the cusp as well as demonstrating that the cusp has sufficient power to fill the ORBE on the timescales of interest. Since a multistep process is only as likely as its lowest probability step, table 4 also demonstrates that the cusp accelerator has the fewest weak links.

Now of course, a quiescent static trap does not accelerate, but in order to understood the dynamics of acceleration, the ground state of the empty, static trap must be understood first. That was the subject of the numerical simulations of SCF2, which showed the trapping limits of the empty (without diamagnetic cavities) equinoctal cusp was rigidity dependent, and matched the energy ranges of both the ring current ions (H^+ <200 eV/nT) as well as the ORBE (e^- <100 keV/nT). Should the cusp be the source of radiation belt electrons and ring current ions, its species dependent energy limits match the observed cutoffs.

In this paper, we show how solar wind transients perturb the static Hamiltonian around an assumed equilibrium (empty cusp) solution, and can provide the changing conditions favorable for acceleration. Accordingly in the "forward-modelling" of section 2, we discuss the quasi-static equilibria of the outer cusp, and the conditions required for stable trapping during a transient. We also discuss the requirements for stochastic acceleration in the cusp, basing it on the more well-understood Fermi-I,II mechanism, and compare this to several interplanetary disturbances. In the "inverse modelling" of section 3, we show how the high-latitude source is consistent with observations of MeV electron injections, and provides a framework for interpreting the statistical correlations.

2 Forward Modelling: The Quasi-Static Cusp

2.1 The Equinoctal Cusp

We traced electrons through a quadrupolar cusp region of a T96 (Tsyganenko and Stern, 1996) magnetosphere for 093 Julian date in IGRF epoch year 2000 at 0000 UT, using a solar wind of 3/cc at 400 km/s and +10nT Bz north ($\equiv Bn$). These conditions are known to be favorable for cusp trapping as we show later. Dst is a nominal +10 nT characteristic of an extended quiet period with little or no ring current, but as we demonstrate later, has little effect on the cusp. We calculated the center of the cusp, q, where the field strength vanishes to be at GSE coordinates (x=6.88, y=-0.04, z=10.1) at a radius r=12.23 Re from the Earth.

Electrons were given initial conditions at various perpendicular radii (0-6 Re), and at various parallel distances (-3 to 1 Re) from this central point at two different MLT "sides" of the cusp, 0000 and 1200 MLT. The particle injection algorithm looped through a range of energies (200-6000 keV) and local pitchangles (70°, 80°, and 90°), or five nested loops altogether. For each starting location, we calculated provisional cusp invariants as follows.

The magnetic moment, $\mu = 1/2mv_\perp^2/|B|$, is the energy in the motion perpendicular to the B-field divided by magnetic field strength. The gyrophase with respect to the B-field was started at 0 for all electrons. The cusp second invariant should be calculated by integrating the parallel velocity along the high-latitude bounce, but instead we used the proxy of the cusp equatorial pitch angle (CEqPA= $\tan^{-1}(v_\perp/v_{||})$) of the particle when it arrives at the high latitude minima on the gyrocenter field line. The bounce phase, s, was taken to be the distance from the cusp equator (field minima $= s_0$) along the fieldline, and was started from -3 Re to +1 Re. Finally, the cusp third invariant should be proportional to the flux enclosed by a drift orbit around the cusp, but without knowing beforehand whether the drift trajectory was closed, we used as a proxy the Euclidean distance from the fieldline minima to the quadrupole center (C-shell=$||s_0 - q||$). The drift phase was the clock angle around the cusp (CLT) relative to the quadrupole null rather than the Earth's surface field, with 1200 CLT being in the plane that included the sun and the B-field vector at the quadrupole null.

In terms of these provisional invariants, the calculated trajectories (details in SCF2 (Glasel et al., 1999; Press et al., 1986)) are classified as "trapped" or "chaotic" based on their ability to drift completely around the cusp following lily-shaped orbits (Sheldon et al., 1998) where we used the approximation that $\tau > 33$ minutes (about two drift orbits) inside a GSE box ((0,20),(-12,12),(-1,20)) is "trapped", whereas $3 < \tau < 33$ minutes are "quasi-trapped". (The approximation is only problematical for low energy electrons, because the T96 B-field is a sum of many current systems, all adding to zero at the quadrupole minima, which leads to large truncation errors near the null point, or a low-resolution discretized B-field whose numerically evaluated gradient can spuriously vanish, as discussed in SCF2.)

In Figure 1 we plot the thousands of electrons traced through the cusp as trapped (blue), quasi-trapped (red), or chaotic (green) in a four panel projection of the 3-D phase space. In the lower left is a 3-axis projection, whereas the remaining panels show projections into two dimensions only. Note that the axes are arranged so that the three 2-D panels can be folded into the sides of a box. From the upper left panel we see that the maximum magnetic moment cutoff for trapping is ~50 keV/nT, with a cusp equatorial pitchangle (CEqPA) ranging from 45°-90°. The minimum magnetic moment cutoff at 3 keV/nT is an artifact of stalling mentioned above, which would vanish (permitting all lower magnetic moments to be trapped) if a better numerical B-field model were used.

The upper right panel shows that the C-shell varies from 1-5 Re, with a high threshold that depends on CEqPA, larger for 90°. The absence of trapping below C-shell$\sim$1 we attribute to the very small $|B|$ near the quadrupole center which destroys the invariants. Note the number of quasi-trapped orbits at large C-shell, which we attribute to the CLT asymmetry of the quadrupole cusp, which is especially shallow at dawn and dusk (Zhou et al., 2006), so that electrons are trapped for less than a full drift orbit.

Finally, the bottom right panel shows a similar quasi-linear dependence of the high C-shell with magnetic moment, larger for smaller magnetic moment. We recognize the same 3 keV/nT numerical limit seen in the left panel. Reference to the lower left panel, shows that the trapped (blue) points form a compact cloud surrounded by untrapped or quasi-trapped orbits, demonstrating that phase space is well-ordered and analytic, that trapping is truly occurring.

Now if these trapped particles pitchangle scatter, they will not change their total energy, but they will change their magnetic moment and simultaneously their 2nd cusp invariant. That is, they will escape the high-latitude minima and travel along the magnetic field line toward the dipole equator. Depending on their CLT, this field line could be on the dayside, around the flanks or down the tail. Alternatively, the cusp could dynamically change its topology due to a solar wind transient, and the high-latitude 2nd invariant could vanish, leading to the same effect as particle pitchangle scattering. Finally, a solar wind transient could betatron energize the particle due to a cusp compression, which may exceed the rigidity-dependent trapping limit in magnetic moment or Cshell. So the instantaneous CLT of the detrapped electron determines whether it ends up in the dipole trap or escaping downtail, while the C-shell determines the final L-shell of the dipole-trapped electrons.

Since the observations of ORBE injections in section 3 are made in the dipole, we need to refine our understanding of the cusp detrapping location. Accordingly, in the next section we examine the dynamics of the cusp trap topology, which control this detrapping point.

2.2 Solar Wind control of Cusp Topology

The MeV electron particle tracing in the equinoctal cusp plot above required thirteen months of CPU time on a 1.8 GHz dual-CPU AMD PC. Therefore computational resources limit the number of cases we can run in order to map out the trapping limits under varied solar wind conditions. It is computationally easy, however, to examine the stable cusp trapping volume to show that the most fragile invariant is often the 2nd (Zhou et al., 2006). That is, the high latitude magnetic minima are often very shallow and strongly dependent on topology. Accordingly we measure the depth of this minima using a T96 magnetic model on a high latitude fieldlines for several solar wind conditions, showing the depth of the minima, $\Delta B_{HI-LAT} = B_{MAX} - B_{MIN}$. This value is then assigned to the footpoint, mapping it to its ionospheric location. Figure 2 shows these high latitude depth mappings for three variables: solar wind pressure, dipole tilt, and Dst, while holding Bn constant, with contours of ΔB at 1, 3, and 10 nT.

Note that there are two pieces of the high latitude minima, the lower latitude "sausage", and the higher latitude "halo". At the midpoint between them lies the quadrupole null where fieldline tracing becomes numerically noisy. The lower latitude minima result from solar wind compression of the subsolar point, whereas the higher latitude minima result from compression on the poleward side of the cusp. These compressions must be mediated by currents, as illustrated by a popular magnetosphere current diagram (Kivelson and Russell, 1995), which shows that the subsolar magnetopause current is dawn-dusk, whereas the poleward cusp current is dusk-dawn, and can be imagined as a Chapman-Ferraro (CF) current "vortex" encircling the cusp in the direction that enhances the subsolar current. This CF vortex current system has the same diamagnetic properties as the ring current, but circulating in the opposite direction from the dipole trapped current. This produces a natural quadrupole with a null magnetic field between the two. It also means that the CF fields are repelled by the ring current, so that increases in dipole $|Dst|$ generate a repulsive force on the cusp, and an expansion of the volume of magnetosphere.

However, the CF vortex and the subsolar current are not a closed system, but parts of a distributed current that can return through the tail or neutral sheet and bypass the cusps altogether. Therefore while coupled, they can change independently. For example, reconnection changes this current system, with Bz southward ($\equiv Bs$) "shorting out" the subsolar current, and Bn affecting the poleward current. Likewise, a tilt of the dipole toward the sun reduces the subsolar current while simultaneously increasing the poleward current. All these changes affect the ability of the cusp to trap particles.

Figure 2 shows that the poleward minima is much more transient than the subsolar minima, and that for negative dipole tilt away from the sun, the "halo" can even completely vanish. This is very significant, because both minima must be present if the trapped particles traced above are to drift completely around the cusp and possess a cusp 3rd invariant. Thus, for some topological configurations of the T96 cusp, there are no cusp trapped particles, and the location where the 2nd invariant is most likely to fail are in the two dawn or dusk boundary regions between the poleward minima and subsolar minima (Zhou et al., 2006).

Figures 3 and 4 show that large $|Dst|$ magnifies the ionospheric footpoint without changing its overall shape. If a halo exists, and a cusp 3rd invariant is still possible, then $|Dst|$ merely enhances the effect without changing the topology. This might be understood by the diamagnetic effect of the CF vortex, causing the CF currents to scale proportional to the ring current, but without changing the topology.

We also note the significant change caused by solar wind pressure. Higher pressure naturally enhances the subsolar current, but under certain conditions also causes the magnetosphere to "flare". That is, Roelof and Sibeck (1993) show that a combination of either Bs and low pressure, or Bn and high pressure cause the sides of magnetosphere to move outward. Since a flared magnetopause tilts the cusp sunward, forcing the poleward currents to enhance, both conditions deepen the poleward minima halo, and enhance the cusp trap. Conversely, Bs weakens the trap, as does low pressure solar wind, whereas Dst has no dynamical effect on the cusp trapping topology, though it may enhance a pre-existing effect.

Therefore, the most likely place for electrons to detrap from a stable configuration when the Bz turns south, or the Earth's tilted dipole rotates away from the Sun, is at the minima observed in Figure 2 on the dawnside at geomagnetic latitude 65° (L=5.6), or on the duskside at geomagnetic latitude 74° (L=13). That is, because the dipole drift of ORBE is clockwise in MLT, the dawnside detrapping electrons will immediately move toward MLT noon, whereas the duskside will move down tail, making the dawnside detrapping spot the most important location for ORBE injections.

2.3 Dipole Appearance of the Injection

Neither the total energy nor the magnetic moment changes as the detrapped electron moves from the cusp to the dipole, which means that the 2nd invariant (parallel energy = total energy - perpendicular) also doesn't change, (Northrop and Teller, 1960). In the cusp trap, the value of the field-invariant, $K = J/\sqrt{2\mu}$, is multivalued, depending on whether one integrates over the dipole equator or just the high latitude minima, we solve by adding all solutions as in Northrop and Teller (1960); Sheldon and Gaffey (1993).

The limited range of K values in the cusp, $K_{MIN} < K < K_{MAX}$, means that the escaping population will have a peculiar pitchangle distribution (PAD) when observed in the dipole trap, appearing as a "butterfly" PAD with a maximum phase space density between 0° and 90°. Since electron detrapping is likely to occur at L=5.5 on the dawnside, we calculate the maximum K (Sheldon and Gaffey, 1993) for cusp-trapped particles at an L=5.5 in a T96 magnetosphere to be 10-15 $\sqrt{nT}$-Re, where $K(s)_{MAX}$ is located at s where $K(s)$ is identical for cusp- and dipole-trapped electrons. This unbiased prediction matches in L-shell and PAD to what is inferred about a non-zero K maximum on CRRES, LANL GEO, and multisatellite studies (Chen et al., 2007a,b; Shprits et al., 2007).

Subsequent radial diffusion into the inner dipole magnetosphere would tend to drive these butterfly PADs toward a 90° peaked or "pancake" PAD, but residues of the butterfly PAD may still be discernible as a dip at 90° (Horne et al., 2003), which is inconsistent with the "flat-topped" distribution expected for 2nd-invariant destroying wave acceleration. Conversely, outward radial diffusion drives these butterfly PADs toward the loss cone, with concommitant precipitation in the atmosphere, so that a low-altitude satellite such as SAMPEX will observe injections as a near-simultaneous injection over L-shells from 3 to 6+ (Baker et al., 1994; Baker et al., 1997; Kanekal et al., 2005).

2.4 Fluctuation Power

Once the cusp possesses a sufficiently deep poleward minima, and a 3rd invariant is possible, then the trap begins to fill and power can injected or extracted from the trap. As discussed in both (Sheldon et al., 1998, 2005), and illustrated by Tables 2 and 3, the three resonant frequencies for MeV electrons in the cusp are approximately 0.1s gyration, 0.5s bounce and 20-200s drift.

Whether due to inaccuracies in particle tracing, magnetic field roundoff errors, or actual chaotic behavior of the particles, the particle tracing gave a range of values for the invariants, to which we have assumed a gaussian spread, (rarely the case), and fit a sigma using the steep side of a skewed distribution, which we also tabulate. When a distribution is double valued, we have used the peak with greater number of events. In all cases, sigma is a minimum estimate, with true distributions having much larger spreads. When no sigma is given, the statistical approach failed, and we estimated the value by another method.

When the bounce period is less than 4 times the gyration period, it becomes difficult to separate them, with the most common error being the misidentification of a half-bounce period as a full bounce, though other "half-harmonics" are also possible. The CEqPA was estimated two ways: the initial pitchangle and local B-field were used with the minimum B-field discovered by tracing the field-line to estimate an initial CEqPA, alternatively, the maximum and minimum B-field encountered in the first 65485 timesteps were used to estimate a "global" minimum CEqPA. While the global value might easily be lower, an underestimate of the initial CEqPA might be attributed to uncertainty in tracing the appropriate B-fieldline in the presence of strong gradients.

Therefore fluctuations in cusp topology or magnetic field in the frequency band between 6mHz-20Hz can couple power to these electrons. In SCF1 we discuss synchronous or resonant fluctuations, in which the disturbance is always going the same direction each time the particle returns to its approximately initial condition. For example, if the cusp were always shrinking, say, by a continually increasing solar wind pressure, then betatron acceleration would energize the particles in the same direction. This has been modeled by (Delcourt et al., 2005) showing significant acceleration. Or if the cusp were always shrinking whenever the particles were at local noon, but expanding at local midnight, then the third drift invariant would be resonant with the cusp disturbance.

The other kind of acceleration discussed in SCF1 is stochastic or non-resonant. In this type of acceleration the cusp compression can occur at all phases and times, so that the population of trapped particles has an equal likelihood of gaining energy as losing. This type of acceleration is diffusive in energy-space, and other things being equal, is less efficient than resonant acceleration. However, it is also more probable, so that the net power can far exceed a resonant mechanism. In terms of the one-dimensional compressive trap found at the bowshock, which accelerates in the $E_{||}$ direction, these two mechanisms are called Fermi-I and Fermi-II (Fermi, 1949; Ellison, 1982; et al., 1990). In our application to the quadrupole trap, the compression is two-dimensional, accelerating in the $E_{\perp}$ direction, and following SCF1 we call it Alfvén-I and Alfvén-II acceleration.

Now the cusp topology responds to both internal and external transients, so that, for example, substorm tail stretching also flares the magnetopause enhancing cusp trapping, whereas substorm dipolarizations detrap so that the 20 minute substorm timescale may couple to the cusp drift resonance through small changes in B. The waves generated by substorms, however, are likely to tranmit more power than these low frequency topology changes, since higher frequency Alfvénic fluctuations should have more Poynting flux, as (Hassam, 1995) has argued, since the cusp is a low-Q absorber for Alfvén waves.

But in terms of sheer power, the internal sources pale in comparison to the solar wind driver. Operating over an area of several square Re on the dayside magnetopause, a sudden fluctuation in solar wind pressure or density changes the CF currents as it pushes the magnetopause in or out. When we consider that the CF currents are immediately adjacent to the cusp and encircle it, then increases in the CF vortex which respond to a 10% increase in solar wind pressure, can cause far more than a 10% energy increase in the cusp trap. Because the magnetopause shrinks in a self-scaling way for certain pressure and Bn regimes (Roelof and Sibeck, 1993), a 10% (∼1 Re) reduction in the subsolar distance would result in a 27% reduction in volume of the cusp trap, magnifying the solar wind fluctuation. Accordingly the cusp trap is an especially sensitive transducer for converting solar wind mechanical energy into fluctuation power for accelerating particles.

Of course, solar wind fluctuation power of the correct resonant frequency will also rapidly accelerate the trapped population. But such peaks in the solar wind fluctuation spectral density are not observed, instead a broad maximum centered near 2mHz indicates that solar wind is structured on a roughly 30 Re spatial scale. Therefore non-resonant processes are more likely to accelerate the trapped particles. In addition, the fluctuations within cusp diamagnetic cavities approach $\Delta B/B \sim 1$, (Chen and Fritz, 1998), while the relative proximity (0.1s/0.5s/100s) of the adiabatic resonances permit diffusion of the invariants, both necessary ingredients for stochastic acceleration.

Note that this transducer is insensitive to solar wind electrical power. That is, the rectified solar wind electric field, Ey=Vx·Bs, causes the magnetopause to trim (not flare), which detraps the cusps. This effectively distinguishes the cusp transducer from the tail transducer, or the mechanical from the electrical response of the magnetosphere. Note also that it is energetic electrons that are trapped in the cusp, not cold electrons, because the existence of the third invariant, like the ring current ions, depends on energetic, ∇B-drift overcoming the $E \times B$-detrapping. Accordingly, this transducer cannot be modelled by MHD, and does not correspond to either Poynting flux or Joule heating. Finally note that our discussion of trapped flux, both in SCF1 and SCF2 has used the statistically generated T96 or T01 models of the magnetospheric cusp, and has not taken into account the observed diamagnetic cavities from POLAR (Chen and Fritz, 2001a; Chen et al., 2001; Chen and Fritz, 2002), which provide feedback from particles trapped in the cusp and change the trap topology.

2.5 Forward Modelling Summary

In summary, the forward modelling of the cusp-trapped electrons shows that they can be trapped for a long enough time for stochastic compressions to accelerate them; that the trapping is sensitive to topology and solar wind conditions; that the detrapping occurs easily with changes in topology at distinct locations, which correspond in L-shell, energy and PADs to observed radiation belt injections; and that there is sufficient power at the broad resonances of the cusp for Arnol'd diffusion to power the process. Many express doubt that such a fragile trap could survive the fluctuations needed to energize particles, but this ignores the positive feedback between the particles in the trap and the trapping magnetic field, which is the topic of a future paper.

3 Inverse Modelling: ORBE from MeV Electron Injections

Having developed a forward modelling of the dynamic behavior of trapped electrons in the cusp and shown that it can explain many of the characteristics of individual radiation belt injections, we now use inverse modelling to infer from the ORBE properties what is the dominant source of radiation belt electrons.

3.1 Prototypical Injection Profile

While this paper was in review, Chen et al. (Chen et al., 2007a,b) and Shprits et al. (Shprits et al., 2007), have argued that their data pinpoint the source region of energetic electrons. More precisely, they have found discrete events that they claim invalidates one leading explanation: the external source. To put their results in context, and to explain its more limited conclusions, we outline the forty year history of radiation belt data.

Recent review papers (Friedel et al., 2002; Dmitriev and Chao, 2003; Vassiliadis et al., 2005) trace the history of the ORBE problem (McIlwain, 1996) that has been recognized since the 1960's. ORBE peak in flux intensity around L∼4, with fluxes rising rapidly over a time span of about 2–3 days, and over an Lshell range $3 < L < 8$. The outer range is approximate, because there is no dipole 3rd invariant at large distances (Roederer, 1970), and because dynamic effects such as magnetopause motion can remove these particles. Later studies (Selesnick and Blake, 1997; Onsager et al., 2004) show that when expressed as phase space density (PSD), the ORBE quiet-time profiles usually show a constant or radially increasing PSD from geosynchronous outward, suggesting an outer boundary source transported rapidly inward. This is consistent with an (externally driven) diffusion rate that varies as $D_{LL} \propto L^{6+}$. Active times are more ambiguous, however, with Hilmer et al. (2000) arguing for an external source beyond L>6.6, while others (Green and Kivelson, 2004; Selesnick and Blake, 2000) arguing for a transient inner (4<L<6) source.

But the origin of the quiet-time or (debated) active-time external source of these MeV electrons was found neither in the solar wind, in the tail, in the magnetosheath, nor on flux tubes connected to Jupiter's MeV electron population. Although isolated events, such as the March 1991 solar wind shock are effective at locally accelerating MeV electrons, the typical MeV event is uncorrelated with shocks, flares, or coronal mass ejections (CME). Conversely, statistical correlations of ORBE injections were found to be poorly correlated ($R < 0.6$) with internal magnetospheric indices: Dst, AE, Kp; as well as poorly correlated with solar wind parameters: Ey, Akasofu's ϵ, B_Z, ρ, ρV^2. The best (simple) correlation to date was found to be V_{SW}, (Paulikas and Blake, 1979), which could produce a linear regression coefficient R ~0.8, but only in a one to two year time span on the declining phase of the solar cycle. (Li et al., 2001b) have pursued these statistics, and with an empirical diffusion model, have managed to achieve R ~0.9 linear correlation coefficients for a one-year span around 1996. (Recent empirical work by Lyatsky (Lyatsky et al., 2007; Lyatsky and Khazanov, 2008) has achieved better correlation coefficients and for longer periods.)

Because the linear correlations have proved so difficult, several non-linear correlations have been examined. Ballatore (2002) using advanced statistical techniques found a solar wind speed threshold of 550 km/s necessary for ORBE effects. (O'Brien et al., 2001) used superposed epoch analysis of Dst minimum, which reached the same conclusions: high speed wind is the most important variable. They argue, however, for an internal source of energy in Pc5 ULF as a secondary correlator. (Vassiliadis et al., 2005) refines this approach, using finite impulse response (FIR) filters keyed to the solar wind velocity to carry out a more extensive search for correlations, which when binned by L-shell, show that the greatest correlator depends on L-shell.

All these statistical studies pointed to an external correlation, and even a typical radial gradient implying an external, but so far, unidentified source. In contrast, theorists have long sought internal sources (Summers and Omura, 2007; Summers et al., 2007b,a), and many experimentalists have pored over satellite data, but the time-space ambiguity of single spacecraft data has heretofore prevented a resolution of temporal versus spatial gradients. This motivated Chen et al. (2007a,b) to study data from multiple spacecraft to make an argument for a spatially resolved peak in the phase space density at L 5, (though without pitchange resolution).

To resolve the pitchangles, they also reanalyzed CRRES data (Shprits et al., 2007) with a Kalman filter to demonstrate that the L=5.5 peak had a $df/dK > 0$ distribution (consistent with butterfly PAD observed by Horne et al. (2003)). Shprits argues that internal sources can be explained by unspecified wave acceleration, but if located in the vicinity of the equator such theories predict a flat-topped rather than butterfly PAD as a consequence of pitchangle diffusion by the same waves ($df/dK \sim 0$ Horne et al. (2003)), not the positive K-gradient Shprits finds. Nor does the theory predict that wave activity should peak outside the plasmapause at L=5.5, nor at high latitude on the field line. So while this discovery may invalidate an exclusive "external source + radial diffusion" explanation, it is weak support for an internal wave acceleration model, and lacks an explanation for the statistical correlations with solar wind that supported the external model.

In contrast, we formulate a causal relationship between the external drivers of "recurrent magnetic storms" due to high speed solar wind and ORBE injections, with a requirement for the peculiar butterfly PADS observed, all through a cusp acceleration mechanism.

3.2 Cusp Trapping

3.3 High Speed Solar Wind Triple Play

As we have established in section 2, the high latitude cusp trap responds very differently to solar wind pressure transients depending on the direction of B_Z, with low-pressure Bs slightly enhancing the trap, but high pressure Bn being the clear winner. Therefore the ICME solar wind transients that cause the largest geoeffective, Dst magnetospheric response, those that have Ey, are often the ones with the weakest MeV production and vice versa (Ballatore, 2002, 2003). With sufficiently large driving, whether Ey or pressure, this clear separation breaks down and many other acceleration pathways are energetically allowed, so that superstorms generate plenty of everything. Therefore this anti-correlation between Dst storms and ORBE injections is most noticeable for weak and moderate storms, as we have suggested before (Sheldon and Spence, 1998), but now we present a model to explain the correlation.

There are more characteristics of high speed solar wind, however, that amplify the ORBE effectiveness of these transients. As the Ulysses mission ably demonstrated, high speed solar wind comes from the solar polar corona, and it is also thought that reconnection in this region generate magnetic fieldline "kinks" that produce the high Alfvénic turbulence of this type solar wind. The combination of high speed, high pressure, and high turbulence is a triple play for the cusp dynamics.

3.3.1 High Pressure

First, the high pressure with Bn give us the flared magnetopause and the enhanced poleward B-field minima. This creates the preconditions of a cusp 3rd invariant necessary for a cusp trap to form, as we discussed earlier. But in addition, Bn also enhances the stability of a cusp 3rd invariant. Since the cusp trap only functions for energetic particles that can ∇B-drift around the quadrupole minima, the presence of an electric potential across the cusp will prevent cold plasma from completing a drift orbit. So a 5 kV change across the cusp becomes a $\sim$5 keV energy threshold for trapping, depending on the topology. Since this is above the 0.1 keV peak in the solar wind electron distribution, not many magnetosheath electrons are trapped (as calculated below).

But increasing solar wind Ey, (or Bs), also increases the electric field across the cusp, which raises the energy threshold, making geoeffective ICME's with strong Ey less likely to cause trapping in the cusp. Conversely, it is possible for Bn to reconnect above the cusp, creating counter-potentials that lower the energy threshold, making Bn more ORBE-effective. Finally, we note that electrons are ubiquitous, and even if solar wind electrons are too cold to be trapped, this does not preclude magnetospheric electrons from collecting in the trap, or suprathermal solar wind electrons found in the non-thermal, powerlaw tails. To demonstrate that high speed solar wind and/or solar wind Ey can abruptly and non-linearly "switch on" the trapping of thermal electrons, we calculate the number of electrons above the "trapping threshold" energy below.

3.3.2 Kinetic Temperature

This is the second way that high speed solar wind improves the trap, since the average kinetic energy is higher so that as the solar wind thermalizes in the magnetosheath, the average temperature of the particles is also higher. Since the fast and slow solar wind interact as they leave the sun, with the fast wind "overexpanding" as it comes out of the coronal hole, the density of the fast wind is less than that of the slow wind and must be corrected for the calculation below. Using an average density of slow wind at 10.3/cc, fast wind at 3.4/cc, with average speeds of 330 km/s and 700 km/s, (Holzer, 1992) the density of the fast wind is found to be inversely proportional to velocity, $n \propto 1/v^\gamma$ with a rough index $\gamma = 1.44$.

Then the number of particles above some velocity threshold for a Maxwellian thermal distribution is (cf. (Abramowitz and Stegun, 1964) formula 7.1.22),

$$F(x, \beta) = n\beta^3 \int_x^\infty v^2 e^{-\beta^2 v^2} dv = n(0.25\sqrt{\pi}[1 - \mathrm{erf}(\beta x)] + 0.5x\beta e^{-\beta^2 x^2}) \quad (1)$$

where erf is the error function, $x \equiv \sqrt{2E/m}$ is the threshold velocity, $\beta \equiv \sqrt{m/2kT}$ is from the isotropic temperature, and n is the normalization to the average density. If we define the ratio of temperatures for fast to slow solar wind as, $\alpha \equiv \sqrt{T_f/T_s}$, then $\beta_f = \alpha\beta_s$. Finally, the relative increase in the number of particles $v > x$ as a function of α and $x\beta$ for fixed energy threshold becomes,

$$P(\alpha, x\beta) \equiv (F_f/\alpha^\gamma - F_s)/F_s \tag{2}$$

where we use α as a proxy for solar wind speed. We tabulate P as a function of α and $E/kT(= 2x^2\beta^2)$ in Table 4.

The negative entries occur when the energy threshold is too low, and the decrease in the peak density of the fast solar wind more than outweighs the increase in the tail, resulting in a net reduction in electron flux. When calculating the relative increase, we divided by the slow solar wind F_s, which may approach zero and result in unphysically large relative increases. One should view these unphysical numbers as simply binary, saturated at "on" or "off". Therefore the transmitted flux is a non-linear function of threshold energy, switching on over a relatively short interval around $E/kT \sim 10 - 20$.

If typical slow solar wind electron temperatures in the sheath are 0.1 keV, then doubly fast (800km/s) solar wind should be somewhere between 0.3-0.4 keV in temperature, depending on polytropic index in the sheath. Data from POLAR/TIDE (Elliott et al., 2001) suggest that the perpendicular velocity for cold hydrogen in the outer cusp region is about 10 km/s, corresponding to 1.2 kV/Re electric fields, if all the perpendicular velocity is driven by electric fields rather than, say, gradient drifts. The particle tracing discussed earlier suggests that typical drift paths around the cusp might be as small as 1 Re diameter, though POLAR found diamagnetic cavities up to 6 Re in diameter (Fritz et al., 2003; Chen et al., 2005b). This gives a range of 1.2 - 7.2 kV for potentials across the cusp, which determines the threshold energy. Then the E/kT parameter is about 12–72 with $\alpha \sim 2$. From Table 4, this gives a relative increase $P(E/kT, \alpha) = [(12, 2), (72, 2)] = [(18.5), (9e10)]$, or from partially open to wide open.

Since the radius of the drift orbit determines the magnitude of E/kT, and the radius is determined primarily by C-shell, which is roughly the distance from the quadrupole null as projected on the magnetopause, then the number of particles that might diffuse across the magnetopause at a given E/kT, is proportional to the annular area, $N \propto A = \pi(\mathrm{Csh}_2^2 - \mathrm{Csh}_1^2) \propto E/kT$. By inspection of Table 4, this further steepens the non-linear relative increase for fast wind, by weighting the higher threshold particles.

Finally, if diamagnetic cavities form in the cusp (CDC), as observed by (Chen et al., 1998; Chen and Fritz, 1998, 2000; Chen et al., 2001; Chen and Fritz, 2002), then the mapping along magnetic field lines from the magnetopause goes around the quadrupole null (now spread out over the CDC), which totally excludes drift orbits from the interior of the CDC (since the $\nabla B \to 0$ in this region). Then transmitted magnetosheath electrons are forced to arrive some distance away from the quadrupole null, with a minimum E/kT cutoff energy. A future paper will discuss the topology changes due to CDC, but here we merely note its amplifying effect on this non-linear switch.

This may explain then, the non-linear change in correlation coefficients when the fast solar wind exceeds 550 km/s (Ballatore, 2002). From the table, this corresponds to an $\alpha \sim 1.5$, with a threshold at $E/kT \sim 12$. For a 0.1 keV slow solar wind temperature scaled to $T_f = \alpha^2 T_s = 0.25keV \rightarrow 3kV$, which from a POLAR/TIDE electric field of 1.2 kV/Re, would correspond to 2.5 Re diameter, or a drift C-shell of about 1.2 Re. While we were not able to trace electrons at this low an energy due to truncation errors in the B-field model, Table 1&2 shows that this Cshell was near the lower limit for stable trapping of 200-1200 keV electrons, and presumably stable for 3 keV electrons as well.

3.3.3 Alfvénic Turbulence

The third base in this triple play is the enhanced Alfvénic turbulence of the high speed solar wind. This turbulence not only preheats the electrons (increasing α in Equation 2 without decreasing n), but more importantly, it appears at the magnetopause as fluctuations in total pressure. And the location where the magnetopause is "softest", like a worn shock absorber, is the cusp. Therefore solar wind turbulence induces large $\Delta B/B$ changes in the cusp, and causes large transverse heating $E_\perp$ (Chen and Fritz, 1998). We have argued above and in SCF1 that stochastic heating, or Alfvén-II acceleration delivers the most power to the trapped particles, so we expect the rise in the energy of the trapped electrons to follow a diffusion timescale, with higher energies requiring a longer time. (Of course, the energy diffusion coefficient depends on the fluctuation power available, so that all energies will rise faster when there is higher turbulence.) If one characterizes the seed energy spectrum as a power law, then this time-dependent energization appears as a convex break in the power law spectrum that moves toward higher energy with time.

If our analysis be correct, that Dst makes no change in the cusp topology or trapping, then our model predicts that Dst should have no correlation with MeV electrons. However, many such correlations have been published, which we discuss in the next section.

3.4 Dst versus MeV storms

There has been some confusion concerning the relation between Dst and ORBE injections. Early work (Nagai, 1988; Koons and Gorney, 1991), showed that Dst was a poor predictor of ORBE, and that of the internal indices, Kp showed the most promise. However, (Reeves, 1998) showed what appeared to be nearly a 100% correlation between the occurrence of Dst storms and appearance of MeV electrons, though he later showed (Reeves et al., 2003) a much smaller correlation with magnitude. Therefore recent studies, such as (O'Brien et al., 2001), argue that $|Dst|$ always precedes the MeV injection, and is a necessary, though not sufficient, condition for ORBE injection, such that we must identify what other necessary elements are missing. (Li et al., 2001a) plot SAMPEX data of MeV electrons versus L-shell and overplot Dst purporting to show a quantitative relation between the magnitude of Dst and the depth of penetration and magnitude of MeV electrons. How can these later correlations be consistent with the earlier lack of correlation?

We think it can be explained by separating the Dst response into two components: 1) solar wind Ey, and 2) solar wind σ_P (dynamic pressure variations). The Dst is a magnetic disturbance roughly caused by trapped keV ions in the ring current about 3 Re from the Earth (Dessler and Parker, 1959; Sckopke, 1966), which can change for two reasons: a) the ring current is carrying more amperes because fresh ions are injected; or, b) the ring current is closer to the Earth. Solar wind Ey tends to do both, injecting ions from the tail through enhanced convection, and pushing the duskside closer to the earth. Note that a linear electric field tends to shift the ring current off center, without necessarily shrinking the radius, which to first order, should change the magnetic disturbance D_{ASYM}, not the D_{SYM} that contributes to the Dst. Incomplete longitudinal coverage of magnetic stations, as well as magnetospheric complexities such as field-aligned currents can make these asymmetric currents appear in the Dst, nevertheless, the major impact of Ey is the injection of convecting plasmasheet ions into the ring current, which occurs over a 1-2 hour period.

In contrast, higher fluctuation power in the solar wind leads to enhanced diffusive transport (Schulz and Lanzerotti, 1974). The inner edge of the ring current, marked by a sharp decrease in ion density (Sheldon and Hamilton, 1993; Sheldon, 1994a), occurs as result of the equilibrium between the ion transport ($\propto$ L) from large L and the loss from charge exchange with atmospheric neutrals ($\propto$ 1/L). When the transport coefficients increase, the inner edge equilibrium moves Earthward, and $|Dst|$ increases (Sandanger et al., 2005). One characteristic of this type of $|Dst|$ injection is a 6-12 hour ragged or gradual increase in $|Dst|$, with none of the abruptness or magnitude of Ey injections. It is only when Dst is averaged over a day or more (Reeves, 1998; Li et al., 2001a), that the two types of Dst injections appear qualitatively similar.

Now we have said that high speed solar wind streams are especially effective at forming the cusp trap, and trapping electrons. Since high speed wind typically has a large fluctuation power, which enhances radial diffusion, it is often correlated with the 2nd type of Dst injection. This is especially true in

(Reeves, 1998) study, or in the oft-quoted 1995-1996 correlation year. High speed wind associated with Bs, will perhaps have an effect on both Dst and ORBE, whereas other sources of solar wind Ey will have negligible effect on ORBE. This can be seen in the superposed epoch analysis of (O'Brien et al., 2001), where a high density solar wind that produces $|Dst|$ is anti-correlated to MeV injections, and likewise, strong Bs that rotates northward, or strong $|B|$ in general are somewhat anti-correlated.

Finally, the high correlation of Dst with inner edge of the radiation belts observed by (Li et al., 2001a) can be a consequence of increased transport, not necessarily injection. Likewise the apparent correlation of Dst with MeV electron flux can also be a consequence of increased transport without injection, since as PSD moves Earthward, the adiabatic energization applied to a falling powerlaw spectrum appears as increased flux. Like Dst then, the two sources of increased flux can be either transport or injection, but their plots do not separate the two.

Therefore the earlier study of geosynchronous PSD (taking out the adiabatic effects on fluxes), which depend on MeV injection rather than transport are correct in not finding a strong Dst correlation, since Dst is a consequence of either Ey or inner magnetospheric transport. However, the intriguing model of (Li et al., 2001b) argues that at least during 1996, a diffusive transport code modulated by solar wind conditions can achieve R$\sim$0.9 in predicting MeV electron fluxes at GEO, suggesting no MeV injection is needed, only an outer magnetospheric transport mechanism.

The major difference between this GEO result using solar wind-driven transport and the SAMPEX inner L-shell result of (Li et al., 2001a) using Dst-driven transport, is that transport outside geosynchronous remains somewhat speculative, since SAMPEX, even with 90 minute L-shell scans, does not observe dynamic MeV electron motion at these L-shells. Nor is there sufficient satellite coverage to get unequivocal simultaneous measurements of MeV electrons at multiple L-shells outside GEO. Furthermore, the (Li et al., 2001b) calculation of a 2–3 day diffusive transport rate is not consistent with $\sim$1 day storm diffusion timescales (Schulz and Lanzerotti, 1974), or SAMPEX daily plots, which show a much faster radial transport rate.

In order to achieve a more observationally consistent 2–3 day transport timescale, then, would require smaller diffusion coefficients and larger radial flux gradients with a large flux at the distant boundary. (Taylor et al., 2004) used the CLUSTER instrumentation to look for these putative large PSD sources and found only 1% of what was predicted. Therefore Li's model with constant MeV electron source at L=11 and transport-limited access to geosynchronous is probably an incorrect simplification of the more general model with a time-variable source, which would permit the 2–3 day timescale to be caused by boundary condition rather than the transport rate, such as in the simulation of (Spjeldvik and Fritz, 1981).

It is this time-variable outer BC model that motivated the Chen et al. (2007a) paper, which excludes a BC explanation for the intervals they analyze. Likewise, the positive K-gradient observed by Shprits et al. (2007) and butterfly PADs seen by Horne et al. (2003) are inconsistent with an outer BC model which should produce negative K-gradient (pancake PADs). Therefore, despite early and continuous attempts to correlate MeV injections with Dst, there is no good model of how this can be accomplished.

3.5 Kp/AE versus MeV indices

Other magnetospheric indices have been examined for ORBE prediction, including Kp and AE. (O'Brien et al., 2001) argue for the presence of ULF Pc5 in the Dst recovery phase, as well as an elevated AE in the recovery phase as indicative of MeV particle enhancements. (Vassiliadis et al., 2005) show that AE only becomes a better predictor than V_{SW} or Kp for L-shells outside geosynchronous. If this is the region of ULF acceleration, it suggests an outer magnetosphere source, possibly consistent with Li's outer boundary condition. AE is measured in the auroral zone, so perhaps it is not surprising that it correlates well in this region, however, if it were the sole source, it should correlate to inner regions of the magnetosphere, what (Vassiliadis et al., 2005) refer to as a "coherent" response, which was not found.

This lack of L-shell coherence might be due to the SAMPEX observations of particle flux in a spectral "window", which would map to different parts of the PSD distribution. That is, diffusive transport connects high energy flux at L=3 with low energy flux at L=7, which should behave coherently if transport is great enough. If, however, the flux SAMPEX observes at $L > 7$ correspond to energies higher than the SAMPEX/PET energy threshold at L=4, it cannot see this coherence. Then it is possible that AE might really be responsible for injecting particles at L=8, but SAMPEX cannot record these particles at L=4, hence the lack of AE-correlation there.

Arguing that the SAMPEX measurements have an L-shell dependent coherence length, makes the conclusion that each L-shell has different solar wind or internal drivers (Vassiliadis et al., 2005) not surprising. Note that solar wind Ey, which we relate to their Bs set of indices, is an external driver, and has difficulty penetrating into the inner magnetosphere. Accordingly, it can produce $\sim$100 keV particles with a strong polar cap electric field, but as these tail electrons convect toward the earth, they divert around the inner magnetosphere. The last closed drift path for various electric field configurations, the Alfvén layer, separates these energized tail particles from trapped magnetosphere particles, which for this energy range lies just inside geosynchronous orbit (lower energy ring current ions penetrate further, perhaps to L=4 (Sheldon, 1994b)). Inside this L-shell, transport is diffusive, requiring violation of the 3rd invariant. Therefore it is also not surprising that above L=6 we see Ey factors being the best correlators, and below L=6 we see diffusive terms, related to V_{SW}, becoming dominant.

At about L<4, Vassiliadis et al. (2005) find a completely different response, one that is not coherent with the $4 < L < 7$ response. This population responds almost immediately to an increase in solar wind speed without the usual 2–3 day delay, and is well correlated with Kp. This correlation is often called the "Dst effect" (Li et al., 1997), whereby the ring current (RC $\propto Dst$) abruptly changes the topology of the inner magnetosphere. Since the additional magnetic pressure of the RC causes the flux tube to "inflate", then like an inner-tube blowout the flux tubes expand outward taking the path of least resistance. However, inside the RC, this inflation increases the magnetic pressure, slightly compressing the flux tubes immediately adjacent. Because particles are conserved, the expansion in volume outside the ring current leads to a decrease in MeV flux while the compression inside the ring current leads to an increase in MeV flux, thus causing the Dst-effect to switch sign at the RC location (Kim et al., 2001). Now the fast, positive correlation of this L<4 region with Ey becomes clear: it is the same adiabatic Dst-effect unrelated to the non-adiabatic increase seen 2–3 days later.

In summary, the AE/Kp effects described in the literature are not correlated to non-adiabatic MeV injections, but to adiabatic (reversible) reconfigurations of the magnetosphere unrelated to the source of MeV particles.

3.6 Pitchangle Distribution of Injections

Since the purpose of this paper is to correlate MeV fluxes with ORBE injections, we will ignore the fast, $\sim$1 day adiabatic shifting of the PSD due to transport, and focus only on the effects that have a 2–3 day risetime and require an injection of MeV electrons. To distinguish between the two effects, we look for characteristics unique to injection. Two key signatures that are relatively unaffected by transport are spectra and pitchangle. Both spectra and pitchangles show the effect of adiabatic energization, as $E_{\perp}$ increases with increasing B-field, but subsequent transport does not change the spectral index or remove features from the pitchangle distribution (PAD). This makes spectral and pitchangle information critical in discerning injection mechanisms.

The asymmetries of the Earth's dipole field, primarily caused by the solar wind compression and tail current stretching, cause energetic particles with differing pitchangles to drift on non-overlapping orbits (Roederer, 1970). This drift shell splitting of MeV electrons, which causes a radial gradient in the flux to map to a butterfly PAD at midnight, and a pancake PAD at noon, is well-known (West et al., 1973) and has been most recently observed and discussed by Selesnick and Blake (2002) using the POLAR data set. However, comparison of model simulations and observations, show that the model, even when initialized with observed data at a single MLT, consistently overpredicts the drift shell splitting actually observed. This overprediction only gets worse with higher Kp as the magnetosphere is compressed by solar wind, as during a high speed stream. The most common explanation given–pitchangle scattering is isotropizing the distribution–would also increase the loss rate, which is not observed. Therefore Selesnick and Blake (2002) suggest that "*This may show that the source location of the relativistic electrons, that is the location where they are accelerated, is distributed in local time.*"

We draw two other conclusions from this paper, that quiet times, without any additional MeV injections, show the strongest drift shell splitting effects, precisely because the distributed source has been turned off. Therefore when large butterfly or pancake PAD are observed, we can either infer that we are observing a quiescent magnetosphere (readily determined from the Kp history), or the peculiarities of the source injection directly. But we cannot conclude that stormtime injections have a fixed PAD at a single local time that subsequently evolves to explain all butterfly PADs observed.

This then leads to the observations of peculiar PADs during a MeV storm injection by Horne et al. (2003). Butterfly PAD are observed for some orbits L>4, E>1MeV, and for all orbits that passed through the equator at large L-shell. They may have been present on all orbits, but higher latitude CRRES orbits cannot observe the near-equatorial pitchangle minima, transforming a butterfly to a "flat-topped" PAD. Whereas wave-particle acceleration can achieve flat-topped PADs, apparently they do not produce butterfly PADs unless the acceleration occurred as "*a result of nonlocal acceleration occurring at higher (lower) latitudes.*" Furthermore, were wave-particle acceleration the explanation, it would have to occur for higher energies only, since "*Inspection of higher resolution data at 0.1L ... shows that there is a pancake at 214 keV and a butterfly distribution at 1.47 MeV all the way between L = 5.05–6.05. Data averaging to achieve a spatial resolution of 0.1 L takes approximately 3 min at L = 4 and 6 min at L = 6. However, it takes the spacecraft more than 1 hour to move between these two locations. Thus we conclude that the energy dependence in the butterfly distributions is not due to time of flight effects.*"

As we argued above, high-latitude acceleration in the cusps meet all the criteria of the observations: an accelerated population off the equator to generate butterfly PAD, a distributed MLT source so as to minimize the drift-shell splitting, and a high-energy, E>1 MeV source. Next we discuss additional data supporting the spectral break around 1 MeV.

3.7 Spectral Breaks

In general, magnetospheric electron populations have a high energy powerlaw tail above some thermal peak (Christon et al., 1989, 1991), the κ-distribution, also named for mathematician Mittag-Leffler a century earlier. Therefore a spectral index is often sufficient to describe the high energy part of the spectra, and is assumed when calculating the average energy of detector bin (Contos, 1997), in a "bow-tie" analysis (Selesnick and Blake, 2000). This spectral index is affected differently by different accelerators, and therefore can provide an important discriminator between mechanisms.

Consider the transport of MeV electrons into the inner magnetosphere through radial diffusion that violates the third invariant but conserves the first. Since $\mu = E_\perp/|B|$ is conserved, then as $|B|$ increases, so must the perpendicular energy. The amount of energization is proportional to $f = B_f/B_i$, the ratio of the final to initial $|B|$. Since a powerlaw spectrum is a straight line in log-log space, multiplying a spectrum by the factor f results in a constant shift of the entire spectrum toward higher energy, without changing the spectral index at all (Meredith et al., 2002; Chen et al., 2005a).

As a second example, consider a constant electric field applied to a region that is inside the tail. All the particles experience a $\Delta \mathrm{E_i}$ electric field that increases the energy by an amount $E = q\Delta \mathrm{E_i}$. In a log-log energy spectrum, this additive term increases the low energy, but has little effect at high energy, making the spectral power law steeper (softer), by decreasing the powerlaw's negative index. Only those particles lower in energy than the thermal peak of the kappa function, only those particles below the powerlaw tail would show a flatter (harder) spectral index, which is opposite to what is generally observed.

A third candidate acceleration is betatron acceleration by dB/dt for electrons inside the substorm current loop. Since the gain in energy is proportional to area enclosed by the gyroorbit(s), higher energy electrons gain proportionally more energy. Ignoring the magnetic gradients, the gyro-radius is $\rho = mv/qB$, so the area, $A \propto 2mE/q^2B^2$. The time for a gyro-orbit, $t \propto 2\pi\rho/v \sim k$, so all energies to first order complete the same number of gyroorbits. Thus betatron acceleration increases the energy by a multiplicative constant, $E_f = E_i[1 + 2m/(q^2B^2)]$. When the gyro-radius is larger than the substorm current loop, the energy gain becomes a constant no longer proportional to the area of the gyroorbit, but long before these GeV energies are reached, the electron has drifted through this dipolarization region. In either case, a constant limiting energy is reached, so that a log-log energy spectrum has a break point and the spectral index steepens (softens) above while remaining constant below that breakpoint. That is, this mechanism should produce a peak in the spectrum, roughly at the energy where the drift time across the wedge is equal to the dipolarization time.

As a general rule of thumb, an acceleration that flattens (hardens) a spectral index generally occurs below a convex spectral break, or peak in the spectrum, and an acceleration that steepens (softens) or leaves unchanged occurs above such a break. (Concave spectral breaks, such as the cosmic ray "ankle", would behave oppositely.) Therefore careful attention to spectral breaks and indices can provide helpful information on the MeV acceleration mechanism.

Many of the MeV electron instruments use shielded solid state detectors that measure integral flux above some energy threshold (Baker et al., 1997), so that we have only a two or three point spectral approximation. With these coarse measures, Bühler et al. (1998); Li et al. (1999); Meredith et al. (2002) show that after the main phase of a Dst storm, the MeV spectral index hardens. This suggests that pure radial diffusion, such as the Li et al. (2001b); Elkington et al. (1999) model, cannot fully account for the acceleration. And any electric field mechanism invoked would have to move the (thermal) peak in the electrons above the 1-2 MeV energy so that hardening of the spectrum could occur below the peak. Adiabatically mapping the 2 MeV geosynchronous data to the tail injection boundary at $L \sim 8$, gives an electric field of $\sim$1 MV, much greater than that observed. Likewise the substorm induction effect, even when coupled with radial diffusion, would not be expected by our simplistic analysis to harden the spectral index at all. Of course, more complex betatron acceleration Ingraham et al. (1999); Kim et al. (2000), which also violate the first and second invariants, might harden the spectra just as wave-particle acceleration can harden the index, but only if the resonance energy peak in the spectrum occurs above our hardened spectra. And finding a candidate wave resonance above 3 MeV is a major challenge to theory.

The integral type instruments also show that the amount of hardening, the ratio of the highest energy channel to the lower channels, will vary from storm to storm but stay constant within a storm. From Baker et al. (1997); Kanekal et al. (2001) (and private communication, Blake 1997), we calculate the hardness ratio of a 60° inclined elliptical satellite "HEO", using the top two integral channels, $E > 1.5, 3.5$ MeV. Table 5 summarizes the results. That is, over the 2–3 day risetime of the MeV fluxes, the hardness ratio, h, rises to a a constant value, $h = h_0(1 - e^{kt})$ (Bühler et al., 1998), which is unique to each storm, and roughly proportional to the size. This temporal coherence suggests a single mechanism operating for the duration of the acceleration time. If it were a resonant acceleration mechanism, we would explain the change in hardness ratio as a energy change of the resonant peak. Accordingly, we should look for the inflection point in the spectra above our energy range, preferably with a higher energy resolution instrument.

The CRRES satellite had excellent spectral data, but we have only been able to estimate a spectral break $E_B > 1.6$ MeV from published data (Meredith et al., 2002). POLAR/HIST (Blake et al., 1995) had the spectral resolution, though not the equatorial orbit. Making the assumption that peculiar PAD distributions do not change the spectral breaks, we can use the POLAR data to search for spectral changes. Selesnick et al. (1997) show a quiescent state of the magnetosphere in early 1996, where we find the 1996.120 injection with a spectral break $\sim$4.4 MeV at 4.5 L. Selesnick and Blake (1997) investigated more dynamic periods in the latter half of 1996 having spectral breaks around $\sim$3.4 MeV at $\sim$6 L. The 1997.010 storm received a great deal of attention, and Selesnick and Blake (1998) showed a spectral break of $\sim$2.7 MeV at 6 L. It is very suggestive that the hardness ratio from integral HEO measurements, and the spectral breaks from POLAR/HIST show similar trends, increasing with storm size.

If we attribute this spectral break to a whistler mode chorus MeV electron acceleration mechanism such as Meredith et al. (2002); Horne et al. (2005), then it corresponds to chorus generating electrons in the 30 keV range. Whereas the 1997 - 1999 storms had significant Dst, the largest MeV event of 1996, the 1996.110 storm, had no discernible Dst event, and therefore, an unlikely candidate for chorus heating. However, it was the largest high speed solar wind event of the year, when two coronal holes that had been pulsing the magnetosphere every 12 days joined together. The conditions for cusp trapping were ideal for this event, suggesting that the spectral breaks observed are a characteristic of the rigidity cutoffs in the cusp trap.

In a later paper, we argue that the storm of 1997.010 with its low energy breakpoint was quite unusual, being an abnormally small Ey-driven MeV storm that produced copious amounts of spectrally soft MeV electron flux, which we attribute to a fortuitous combination of winter solstice, diurnal tilt, and solar wind density, that promoted cusp feedback. But for recurrent storms driven by high-speed V_{SW} with E>3 MeV breakpoints, and especially without Dst-correlated chorus waves, there doesn't appear to be any wave explanation.

In summary, the data show spectral hardening inconsistent with either an external source diffusing inward, or an internal source of kV acceleration. Rather, the spectral break occurs at several MeV, requiring either an unlikely wave resonance at high energy (which is coincidently correlated to storm size), or more likely, a magnetic trap with a rigidity cutoff at several MeV correlated with solar wind pressure, such as the outer cusp.

3.8 Inverse Modelling Summary

In summary, the statistics of MeV injections show that the 2–3 day injection is not caused by transport delay, but by a source delay; that it is not at a single MLT but distributed over a sector; that it is not equatorially energized but accelerated at high latitude; that it has a spectral breakpoint at several MeV, higher for more intense solar wind drivers; that spectral hardening excludes betatron and radial diffusion as acceleration sources; and that internal magnetic activity $AE/Kp/Dst$ is uncorrelated to the source region. These are all the inferred properties of the source, while our deduced properties of the cusp show that this source would be correlated with high speed solar wind but not internal magnetic indices; would have a butterfly PAD; would be distributed in MLT; would appear as a PSD peak no further out than L=5.5 (compressions could bring it in); would appear at LEO as a simultaneous precipitation over many L-shells; would demonstrate seasonal (dipole tilt) effects; would harden the spectral index below the breakpoint; and would have a solar wind dependent breakpoint (hardening below, softening above) caused by the rigidity cutoff around 3 MeV.

4 Conclusions

In this paper, we have continued our earlier work on the static trapping properties of the cusp, to show how these energy and pitchangle limits map to the ORBE dipole trap through dynamic transport, which would leave a unique fingerprint in the energy spectral index, butterfly PAD and time-delayed statistical correlations. We also showed how high speed solar wind streams would have a non-linear coupling both to the trapping and energizing of electrons.

We compare these predictions based on the physics of the cusp topology with the statistics collected from over 40 years of ORBE observations, to demonstrate the remarkable correlations. In particular, this high latitude source naturally resolves many puzzling aspects of the injections not explained by an external boundary source model, including a distant yet internal magnetospheric source, a distributed MLT injection, a strongly butterfly PAD, a high energy spectral break, a better correlation to V_{SW} than Ey or other energy-derived indices, a 2–3 day risetime, and the lack of an ionic, Dst correlation. And while an internal (non-cusp) source can be arbitrarily located (off-equatorial, L=5.5, distributed MLT) and arbitrarily triggered ($V_{SW} > 550$km/s, Bn, resonant $E \propto V_{SW}$, 2 day delay) so as to explain many of these observations, it may be difficult to satisfy all conditions simultaneously without additional ad hoc assumptions not needed by the cusp model.

While the quiescent cusp we model didn't inject to L-shells as low as observed (L=3 during major storms), future studies will include a more compressed magnetopause as well as the positive feedback engendered by trapped plasma in the cusp. Both of these effects will deepen the cusp minima, and therefore increase both the trapping and the minimum L-shell expected for detrapped cusp electrons. In addition, more recent magnetic field models such as TS05 have substorm currents included, which may both affect the static equilibrium as well as the dynamics of detrapping. It should be noted that, although the cusp-source theory may explain many features, it still lacks the direct supporting observational evidence, which we hope will be supplied by the upcoming RBSP mission, to confidently assert this cusp-source theory is superior to other theories. The purpose of this paper, however, was to demonstrate the likelihood of a cusp source for MeV radiation belt injections.

Acknowledgments

We acknowlege fruitful conversations with colleagues at NASA/MSFC/NSSTC and NASA grants NAG-5 2578, NAG-5 7677, and NAG-5 1197 at Boston University. Figures 2-4 were the work of UAH masters student, Ravi Kinera, and Table 4 in large part to NSSTC colleague Emmanuel Krivorutsky, and particle tracing code is indebted to Jim Sullivan.

References

Abramowitz, M., Stegun, I., 1964. Handbook of Mathematical Functions with Formulas, Graphs, and Mathematical Tables. Vol. National Bureau of Standards Applied Mathematics Series 55. U.S. Government Printing Office, Washington, DC.

Baker, D. N., Blake, J. B., Callis, L. B., Cummings, J. R., Hovestadt, D., Kanekal, S., Klecker, B., Mewaldt, R. A., Zwickl, R. D., Mar. 1994. Relativistic electron acceleration and decay time scales in the inner and outer radiation belts: SAMPEX. Geophys. Res. Lett. 21, 409–412.

Baker, D. N., Blake, J. B., Klebesadel, R. W., Higbie, P. R., 1986. Highly relativistic electrons in the earth's outer magnetosphere 1. lifetimes and temporal history 1979–1984. J. Geophys. Res. 91, 4265–4276.

Baker, D. N., Li, X., Turner, N., Allen, J. H., Bargatze, L. F., Blake, J. B., Sheldon, R. B., Spence, H. E., Belian, R. D., Reeves, G. D., Kanekal, S. G., Klecker, B., Lepping, R. P., Olgivie, K., Mewaldt, R. A., Onsager, T., Singer, H. J., Rostoker, G., 1997. Recurrent geomagnetic storms and relativistic electron enhancements in the outer magnetosphere: ISTP coordinated measurements. J. Geophys. Res. 102, 14,141–14,148.

Ballatore, P., 2002. Effects of fast and slow solar wind on the correlations between interplanetary medium and geomagnetic activity. J. Geophys. Res. 107 (A9, 1227).

Ballatore, P., 2003. Reply to Comment on "Effects of fast and slow solar wind on the correlations between interplanetary medium and geomagnetic activity" by C. B. Wang and J. K. Chao. J. Geophys. Res. 108 (A10, 1387).

Blake, J. B., Fennell, J. F., Friesen, L. M., Johnson, B. M., Kolasinski, W. A., Mabry, D. J., Osborn, J. V., Penzin, S. H., Schnauss, E. R., Spence, H. E., Baker, D. N., Belian, R., Fritz, T. A., Ford, W., Laubsher, B., Stiglich, R., Baraze, R. A., Hilsenrath, M. F., Imhof, W. L., Kilner, J. R., Mobilia, J., Voss, D. H., Korth, A., Güll, M., Fisher, K., Grande, M., Hall, D., 1995. CEPPAD: Comprehensive energetic particle and pitch angle distribution experiment on POLAR. In: Russell, C. T. (Ed.), The Global Geospace Mission. Kluwer Academic Publishers, pp. 531–562.

Bühler, P., Johnstone, A., Desorgher, L., Zehnder, A., Daly, E., Adams, L., 1998. The outer radiation belt during the 10 January, 1997 CME event. Geophys. Res. Lett. 25 (15), 2983–2986.

Chang, S.-W., 1998. Cusp energetic ions: a bow shock source. Geophys. Res. Lett. 25, 3729–3732.

Chang, S.-W., Scudder, J. D., Kudela, K., Spence, H. E., Fennell, J. F., Lepping, R. P., Lin, R. P., Russell, C. T., 2001. MeV magnetosheath ions energized at the bow shock. J. Geophys. Res. 106, 19101–19115.

Chen, J., Fritz, T. A., 1998. Correlation of cusp mev helium with turbulent ulf power spectra and its implications. Geophys. Res. Lett. 25, 4113–4116.

Chen, J., Fritz, T. A., 2000. Origins of energetic ions in cep events and their implications. Int. J. Geomagn. Aeron. 2, 31.

Chen, J., Fritz, T. A., 2001a. Energetic oxygen ions of ionospheric origin observed in the cusp. Geophys. Res. Lett. 28 (8), 1459–1462.

Chen, J., Fritz, T. A., 2001b. Features of energetic ions near the compressed magnetosphere. J. Atm. Solar-Terrestrial Phys. 63, 463–472.

Chen, J., Fritz, T. A., 2002. The global significance of the cep events. In: Wang, H. N., Xu, R. L. (Eds.), Solar-Terrestrial Magnetic Activity and Space Environment. Vol. Cospar Colloq. Ser 14. pp. 239–249.

Chen, J., Fritz, T. A., Sheldon, R. B., 2005a. Comparison of energetic ions in cusp and outer radiation belt. J. Geophys. Res. 110 (A12219).

Chen, J., Fritz, T. A., Sheldon, R. B., 2005b. Multiple spacecraft observations of energetic ions during a high solar wind pressure event. J. Geophys. Res. 110 (A12212).

Chen, J., Fritz, T. A., Sheldon, R. B., Pickett, J. S., Russell, C. T., 2001. The discovery of a new acceleration and possible trapping region of the magnetosphere. Adv. Space Res. 27 (8), 1417–1422.

Chen, J., Fritz, T. A., Sheldon, R. B., Spence, H. E., Spjeldvik, W. N., Fennell, J. F., Livi, S., 1997. A new temporarily confined population in the polar cap. Geophys. Res. Lett. 24, 1447–1450.

Chen, J., Fritz, T. A., Sheldon, R. B., Spence, H. E., Spjeldvik, W. N., Fennell, J. F., Livi, S., Russell, C., Gurnett, D., 1998. Cusp energetic particle events: Implications for a major acceleration region of the magnetosphere. J. Geophys. Res. 103, 69–78.

Chen, Y., Friedel, R. H. W., Reeves, G. D., Cayton, T. E., Christensen, R., Nov. 2007a. Multisatellite determination of the relativistic electron phase space density at geosynchronous orbit: An integrated investigation during geomagnetic storm times. Journal of Geophysical Research (Space Physics) 112 (A11), 11214–+.

Chen, Y., Reeves, G. D., Friedel, R. H. W., Sep. 2007b. The energization of relativistic electrons in the outer Van Allen radiation belt. Nature Physics 3, 614–617.

Christon, S. P., Williams, D. J., Mitchell, D. G., Frank, L. A., Huang, C. Y., 1989. Spectral characteristics of plasma sheet ion and electron populations during undisturbed geomagnetic conditions. J. Geophys. Res. 94, 13409–13424.

Christon, S. P., Williams, D. J., Mitchell, D. G., Huang, C. Y., Frank, L. A., 1991. Spectral characteristics of plasma sheet ion and electron populations during disturbed geomagnetic conditions. J. Geophys. Res. 96, 1–22.

Contos, A. R., 1997. Complete description and characterization of the high sensitivity telescope (hist) onboard the polar satellite. Master's thesis, Boston University, Boston, MA.

Delcourt, D. C., Malova, H. V., Zelenyi, L. M., Sauvaud, J.-A., Moore, T. E., Fok, M.-C., 2005. Energetic particle injections into the outer cusp during compression events. Earth Planets Space 57 (2), 125–130.

Dessler, A. J., Parker, E. N., 1959. Hydromagnetic theory of geomagnetic storms. J. Geophys. Res. 64, 2239.

Dmitriev, A. V., Chao, J. K., 2003. Dependence of geosynchronous relativistic electron enhancements on geomagnetic parameters. J. Geophys. Res. 108 (A11, 1388).

Elkington, S. R., Hudson, M. K., Chan, A. A., 1999. Acceleration of relativistic electrons via drift-resonant interaction with toroidal-mode pc-5 ulf oscillations. Geophys. Res. Lett. 26, 3273–3276.

Elliott, H. A., Comfort, R. H., Craven, P. D., Chandler, M. O., Moore, T. E., 2001. Solar wind influence on the oxygen content of ion outflow in the high-altitude polar cap during solar minimum conditions. J. Geophys. Res. 106 (A4), 6067–6084.

Ellison, D. C., march 1982. Monte Carlo Simulation of Collisionless Shock Acceleration. Ph.D. thesis, AA (The Catholic University of America).

et al., D. C. E., 1990. Particle injection and acceleration at Earth's bow shock: Comparison of upstream and downstream events. Astrophys. J. 352.

Fermi, E., 1949. Phys. Rev. 75, 1169.

Friedel, R. H., Reeves, G. D., Obara, T., 2002. Relativistic electron dynamics in the inner magnetosphere–a review. J. Atm. Solar-Terrestrial Phys. 64, 265–282.

Fritz, T. A., Chen, J., Siscoe, G. L., 2003. Energetic ions, large diamagnetic cavities, and Chapman-Ferraro cusp. J. Geophys. Res. 108 (A1).

Glasel, J., Sullivan, J. D., Fritz, T. A., 1999. EOS Trans. Suppl SM32D-10, S283.

Green, J. C., Kivelson, M. G., 2004. Relativistic electrons in the outer radiation belt: Differentiating between acceleration mechanisms. J. Geophys. Res. 109 (A03213).

Hassam, A. B., 1995. Dynamics and dissipation of compressional alfven waves near magnetic nulls. Phys. Plasmas 2 (12), 4662–4664.

Hilmer, R. V., Ginet, G. P., Cayton, T. E., 2000. Enhancement of equatorial energetic electron fluxes near L = 4.2 as a result of high-speed solar wind streams. J. Geophys. Res. 105, 23,311–23,322.

Holzer, T. E., 1992. Interplanetary medium, solar wind. In: Maran, S. P. (Ed.), The Astronomy and Astrophysics Encyclopedia. Cambridge University Press, Cambridge, pp. 336–338.

Horne, R. B., Meredith, N. P., Thorne, R. M., Heynderickx, D., Iles, R. H. A., Anderson, R. R., 2003. Evolution of energetic electron pitch angle distributions during storm time electron acceleration to megaelectronvolt energies. J. Geophys. Res. 108 (A1, 1016).

Horne, R. B., Thorne, R. M., Glauert, S. A., Albert, J. M., Meredith, N. P., Anderson, R. R., 2005. Timescale for radiation belt electron acceleration by whistler mode chorus waves. J. Geophys. Res. 110 (A03225).

Ingraham, J., Belian, R. D., Cayton, T. E., Meier, M. M., Reeves, G. D., 1999. March 24, 1991, geomagnetic storm: Could substorms be contributing to relativistic electron flux buildup at geosychronous altitude? Eos Supplement 80, S294.

Kanekal, S. G., Baker, D. N., Blake, J. B., 2001. Multisatellite measurements of relativistic electrons: Global coherence. J. Geophys. Res. 106 (A12), 29,721–29,732.

Kanekal, S. G., Friedel, R. H. W., Reeves, G. D., Baker, D. N., Blake, J. B., Dec. 2005. Relativistic electron events in 2002: Studies of pitch angle isotropization. Journal of Geophysical Research (Space Physics) 110 (A9), 12224–+.

Kim, H.-J., Chan, A. A., Wolf, R. A., Birn, J., 2000. Can substorms produce relativistic outer belt electrons? J. Geophys. Res. 105, 7721.

Kim, H.-J., Rostoker, G., Kamide, Y., 2001. Radial dependence of relativistic electron fluxes for storm main phase development. J. Geophys. Res. 107 (A11, 1378).

Kivelson, M. G., Russell, C. T., 1995. Introduction to Space Physics. New York: Cambridge University Press.

Koons, H. C., Gorney, D. J., 1991. A neural network model of the relativistic electron flux at geosynchronous orbit. J. Geophys. Res. 96, 5549–5556.

Li, X., Baker, D. N., Kanekal, S. G., Looper, M., Temerin, M., October 15 2001a. Long term measurements of radiation belts by sampex and their variations. Geophys. Res. Lett. 28 (20), 3827–3830.

Li, X., Baker, D. N., Temerin, M., Cayton, T. E., Reeves, E. G. D., Christensen, R. A., Blake, J. B., Looper, M. D., Nakamura, R., Kanekal, S. G., 1997. Multisatellite observations of the outer zone electron variation during the november 3–4, 1993, magnetic storm. J. Geophys. Res. 102 (A7), 14,123–14,140.

Li, X., Baker, D. N., Temerin, M., Cayton, T. E., Reeves, G. D., Selesnick, R. S., Blake, J. B., Lu, G., Kanekal, S. G., Singer, H. J., 1999. Rapid enhancements of relativistic electrons deep in the magnetosphere during the May 15, 1997, magnetic storm. J. Geophys. Res. 104 (A3), 4467–4476.

Li, X., Temerin, M., Baker, D. N., Reeves, G. D., Larson, D., May 1 2001b. Quantitative prediction of radiation belt electrons at geostationary orbit based on solar wind measurements. Geophys. Res. Lett. 28 (9), 1887–1890.

Lyatsky, W., Khazanov, G. V., Feb. 2008. Effect of solar wind density on relativistic electrons at geosynchronous orbit. Geophys. Res. Lett. 35, 3109–+.

Lyatsky, W., Lyatskaya, S., Tan, A., Jan. 2007. A coupling function for solar wind effect on geomagnetic activity. Geophys. Res. Lett. 34, 2107–+.

McIlwain, C. E., 1996. Processes acting upon outer zone electrons. In: et. al, J. F. L. (Ed.), Radiation Belts Models and Standards. AGU, Washington DC.

Meredith, N. P., Horne, R. B., Summers, D., Thorne, R. M., Iles, R. H. A., Heynderickx, D., Anderson, R. R., 2002. Evidence for acceleration of outer zone electrons to relativistic energies by whistler mode chorus. Ann. Geophys. 20, 967–979.

Nagai, T., 1988. "space weather forecast": Prediction of relativistic electron intensity at synchronous orbit. Geophys. Res. Lett. 15, 425–428.

Northrop, T. G., Teller, E., 1960. Stability of the adiabatic motion of charged particles in the earth s field. Phys. Rev. 117, 215.

O'Brien, T. P., McPherron, R. L., Sornette, D., Reeves, G. D., Friedel, R., Singer, H. J., 2001. Which magnetic storms produce relativistic electrons at geosynchronous orbit? J. Geophys. Res. 106 (A8), 15533–15544.

Onsager, T. G., Chan, A. A., Fei, Y., Elkington, S. R., Green, J. C., Singer, H. J., 2004. The radial gradient of relativistic electrons at geosynchronous orbit. J. Geophys. Res. 109 (A05221).

Paulikas, G. A., Blake, J. B., 1979. Effects of the solar wind on magnetospheric dynamics: Energetic electrons at geosynchronous orbit. In: Olson, W. P. (Ed.), Quantitative Modelling of Magnetospheric Processes, Geophys. Monogr. Ser. Vol. 21. AGU, Washington, D.C., p. 180.

Press, W. H., Teukolsky, S. A., Vetterling, W. T., Flannery, B. P., 1986. Numerical Recipes: The art of scientific computing. Cambridge Univ. Press, Cambridge.

Reeves, G. D., 1998. Relativistic electrons and magnetic storms: 1992-1995. Geophys. Res. Lett. 25, 1817–1820.

Reeves, G. D., McAdams, K. L., Friedel, R. H. W., O'Brien, T. P., May 2003. Acceleration and loss of relativistic electrons during geomagnetic storms.

Geophys. Res. Lett. 30, 36–1.

Roederer, J. G., 1970. Dynamics of Geomagnetically Trapped Radiation. Springer, New York.

Roelof, E., Sibeck, D. G., December 1993. Magnetopause shape as a bivariate function of interplanetary magnetic field b_z and solar wind dynamic pressure. J. Geophys. Res. 98 (A12), 21,421–21,450.

Sandanger, M. I., Soraas, F., Aarsnes, K., Oksavik, K., Evans, D. S., Greer, M. S., 2005. Proton injections into the ring current associated with b_z variations during HILDCAA events. In: Physics and Modeling of the Inner Magnetosphere. Vol. AGU Monograph. Helsinki Chapman conf 2003.

Schulz, M., Lanzerotti, L. J., 1974. Particle Diffusion in the Radiation Belts. Springer-Verlag, New York.

Sckopke, N., 1966. A general relation between the energy of trapped particles and the disturbance field near the earth. J. Geophys. Res. 71, 3125.

Selesnick, R. S., Blake, J. B., 1997. Dynamics of the outer radiation belt. Geophys. Res. Lett. 24 (11), 1347–1350.

Selesnick, R. S., Blake, J. B., 1998. Radiation belt electron observations following the january 1997 magnetic cloud event. Geophys. Res. Lett. 25 (14), 2553–2556.

Selesnick, R. S., Blake, J. B., 2000. On the source location of radiation belt relativistic electrons. J. Geophys. Res. 105, 2607–2624.

Selesnick, R. S., Blake, J. B., 2002. Relativistic electron drift shell splitting. J. Geophys. Res. 107 (A9, 1265).

Selesnick, R. S., Blake, J. B., Kolasinski, W. A., Fritz, T. A., 1997. A quiescent state of 3 to 8 mev radiation belt electrons. Geophys. Res. Lett. 24 (12), 1343–1346.

Sheldon, R. B., 1994a. Ion transport and loss in the earth's quiet ring current 2. diffusion and magnetosphere-ionosphere coupling. J. Geophys. Res. 99, 5705–5720.

Sheldon, R. B., 1994b. Plasmasheet convection into the inner magnetosphere during quiet conditions. In: Baker, D. N. (Ed.), Solar Terrestrial Energy Program: COSPAR Colloquia Series. Vol. 5. Pergamom Press, New York, pp. 313–318.

Sheldon, R. B., Fritz, T. A., Chen, J., 2005. The quadrupole as a source of energetic particles: I. general considerations. In: Gallagher, D., Horwitz, J., Perez, J., Preece, R., Quenby, J. (Eds.), Particle Acceleration in Astrophysical Plasmas: Geospace and beyond. Vol. AGU Monograph 156. pp. 197–204.

Sheldon, R. B., Fritz, T. A., Chen, J., 2006. The quadrupole as a source of energetic particles: Ii. the static equinoctal cusp, presented at Huntsville Workshop 2004.

Sheldon, R. B., Gaffey, Jr, J. D., 1993. Particle tracing in the magnetosphere: New algorithms and results. Geophys. Res. Lett. 20, 767–770.

Sheldon, R. B., Hamilton, D. C., 1993. Ion transport and loss in the earth's quiet ring current 1. data and standard model. J. Geophys. Res. 98, 13,491–

13,508.

Sheldon, R. B., Spence, H. E., 1998. A new magnetic storm model. In: Horwitz, J. (Ed.), Geospace Mass and Energy Flow: Results from the International Solar-Terrestrial Physics Program. AGU, Washington, D.C., pp. 349–354.

Sheldon, R. B., Spence, H. E., Sullivan, J. D., Fritz, T. A., Chen, J., 1998. The discovery of trapped energetic electrons in the outer cusp. Geophys. Res. Lett. 25, 1825–1828.

Shprits, Y., Kondrashov, D., Chen, Y., Thorne, R., Ghil, M., Friedel, R., Reeves, G., Dec. 2007. Reanalysis of relativistic radiation belt electron fluxes using CRRES satellite data, a radial diffusion model, and a Kalman filter. Journal of Geophysical Research (Space Physics) 112 (A11), 12216–+.

Spjeldvik, W. N., Fritz, T. A., 1981. Observations of energetic helium ions in the earth's radiation belts during a sequence of geomagnetic storms. J. Geophys. Res. 86, 2317.

Summers, D., Ni, B., Meredith, N. P., apr 2007a. Timescales for radiation belt electron acceleration and loss due to resonant wave-particle interactions: 1. Theory. Journal of Geophysical Research (Space Physics) 112 (A11), 4206–+.

Summers, D., Ni, B., Meredith, N. P., apr 2007b. Timescales for radiation belt electron acceleration and loss due to resonant wave-particle interactions: 2. Evaluation for VLF chorus, ELF hiss, and electromagnetic ion cyclotron waves. Journal of Geophysical Research (Space Physics) 112 (A11), 4207–+.

Summers, D., Omura, Y., dec 2007. Ultra-relativistic acceleration of electrons in planetary magnetospheres. Geophys. Res. Lett. 34, 24205–+.

Taylor, M. G. G. T., Friedel, R. H. W., Reeves, G. D., Dunlop, M. W., Fritz, T. A., Daly, P. W., Balogh, A., 2004. Multisatellite measurements of electron phase space density gradients in the earth's inner and outer magnetosphere. J. Geophys. Res. 109 (A05220).

Tsyganenko, N. A., Stern, D. P., 1996. Modeling the global magnetic field of the large-scale Birkeland current systems. J. Geophys. Res. 101, 27187–27198.

Vassiliadis, D., Fung, S. F., Klimas, A. J., 2005. Solar, interplanetary, and magnetospheric parameters for the radiation belt energetic electron flux. J. Geophys. Res. 110 (A04201).

West, Jr, H. I., Buck, R. M., Walton, R. J., 1973. Electron pitch angle distributions throughout the magnetosphere as observed by OGO 5. J. Geophys. Res. 78, 1064.

Zhou, X.-Z., Fritz, T. A., Zong, Q.-G., Pu, Z. Y., Hao, Y.-Q., Cao, J.-B., Nov. 2006. The cusp: a window for particle exchange between the radiation belt and the solar wind. Annales Geophysicae 24, 3131–3137.

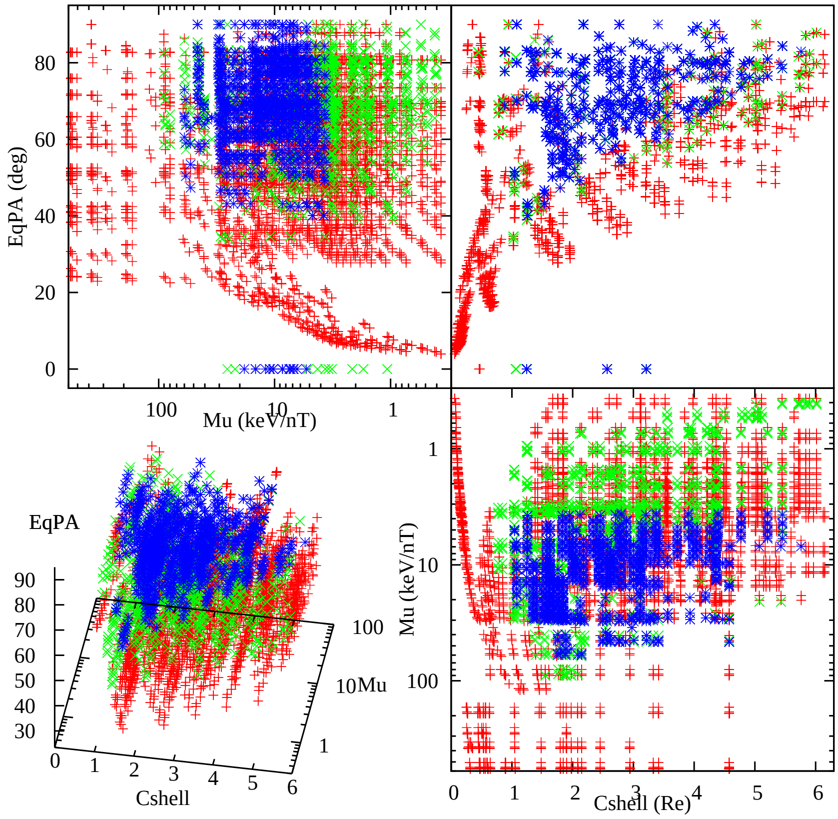

Fig. 1. Electron trajectory phase space mapping in provisional cusp invariants: Red are chaotic, green quasi-trapped and blue trapped.

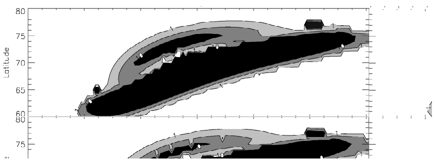

Fig. 2. High latitude minima depth mapped to ionospheric latitude and longitude. Contours are at 1, 3, and 10 nT: columns at -3.7, +1.7, and +7.3 degrees dipole tilt toward sun; rows from top at 5, 3.3, 1.7 nPa dynamic pressure of solar wind.

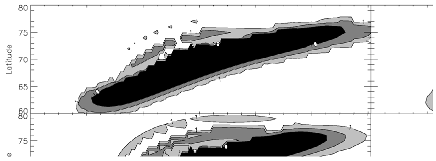

Fig. 3. Minima contours with columns at -3.7, +1.7 and +7.3 degrees dipole tilt, rows from top at -50, -30, and -10 nT Dst.

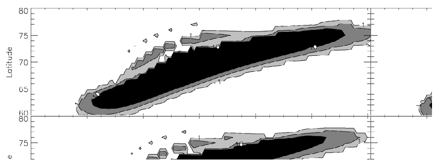

Fig. 4. Minima contours with columns at 1.7, 3.3, and 5 nPa dynamic pressure solar wind, rows from top at -50, -30, -10 nT Dst

.

Table 1
Comparison of Three Traps

Feature	Dipole	Fermi	Quadrupole
1)Stochasticity $\tau_1/\tau_2/\tau_3$	poor .001:1:1000	moderate $.001{:}> 10^3{:}> 10^4$	**good** .1:1:10
2)Process flow	poor rim-fed, ctr-exit exit blocked	moderate end-fed, side-exit exit diffusion	**good** ctr-fed, rim-exit exit rapid
3)Wave coupling	poor hi E decoupled	moderate all E coupled	**good** hi E coupled
4)Trap vs. accel. accel.	moderate traps	poor detraps	**good** traps/releases
5)Free of Diffusion	poor no accel. w/o	moderate increases E_{max}	**good** insignificant
6)Adiabatic heating PAD	**good** 2D pancake	moderate 1D cigar	**good** 2D pancake
7)Energy sources	external SW compress	external SW Alfvén wave	**ext.+int.** SW + substorms
8a)electron E_{max} MeV	**good** 900 w/ 10Re	poor 1.8 w/ 0.1 Re	moderate 280 w/ 3 Re
8b) electron E_{min} keV	poor < 45	**good** 2.5	moderate 30
9a)Trap volume m^3	**good** 10^{24}	poor 10^{20}	moderate 10^{22}
9b)Trap lifetime sec	**good** $> 10^{13}$	poor $10^4 s$	moderate lo:hi $10^9{:}10^5$
9c)Accel. time sec	poor >300,000	**good** 8,000	moderate 25,000
9d)Trap Power Watts	**good** $< 5 \times 10^8$	poor 10^6	moderate 5×10^7
10) 2day ORBE inj. freq. freq.	poor <0.576	**good** 22	moderate 7
11) ORBE Prob (norm) W/sec	moderate <1700	poor 160	**good** 2000

Table 2
Selected Cusp-Trapped Electron Timescales.

Energy MeV	Gyration τ_1 ms	Bounce τ_2 ms	Drift τ_3 sec	μ keV/nT	CEqPA Deg	Cshell Re
0.2	87+41	186+22	8.08+.44	28.1+1.3	61.2/60.1	0.77
0.2	71+18	1255+475	241	10.08+.16	82.9/77.7	2.42
0.2	44.6+6.3	679+644	328	9.22+.10	80.5/76.5	3.43
0.2	38.1+5.5	697+610	564	7.98+.10	80.2/79.4	4.22
0.2	36.8+7.7	670+590	1130	7.28+.22	80.4/79.7	4.91
0.4	12.1+3.4	305+26	69.0+1.8	18.48+.41	40.1/51.2	1.26
0.4	12.1+3.3	460+24	368	13.99+.14	49.2/55.6	2.12
0.4	22.2+3.4	90+72	13.02+.40	42.4+1.1	82.7/69.9	1.31
0.4	11.7+3.0	215+48	132	20.10+.28	82.9/77.1	2.42
0.4	17.5+4.4	182+40	103	18.32+.37	76.5/74.6	3.54
0.4	11.9+3.2	214+35	176	15.86+.45	80.3/75.3	4.22
0.4	10.1+1.9	288+24	384	14.38+.29	80.4/77.2	4.91
0.6	28.4+7.5	710+200	49+2	25.34+.61	40.1/50.9	1.26
0.6	24.2+5.0	500+140	63.6	30.22+.63	56.4/58.3	1.83
0.6	122+50	400+140	9.1+1.1	62.6+1.7	82.7/65.9	1.31
0.6	112+35	280+100	95.4+1.6	30.27+.61	82.9/73.5	2.42
0.6	75+30	300+24	128	27.60+.36	80.5/74.3	3.43
0.6	58+13	360+20	221	23.94+.50	80.3/74.5	4.22
0.6	91+32	310+90	333	21.78+.74	80.4/74.9	4.91
0.8	34.5+7.0	342+90	37.6+3.3	37.3+1.1	40.1/50.9	1.26
0.8	34.2+6.8	630+140	70.5+1.1	35.29+.52	51.5/56.0	1.83
0.8	112+43	185+62	6.0+1.2	85.2+4.3	82.8/62.3	1.31
0.8	37.3+8.7	65+20	74.5+1.5	40.04+.54	82.9/73.9	2.42
0.8	30.4+9.4	64+19	101.2+1.3	36.48+.84	80.5/73.6	3.43
0.8	28.1+6.7	231+58	173	32.0+1.1	80.3/74.8	4.22
0.8	29.9+7.8	430+96	326	28.82+.87	80.4/74.6	4.91
1.0	38+12	545+59	32.2+1.6	47.1+1.9	40.1/45.5	1.26
1.0	46+16	567+59	57.4+1	44.4+1.3	51.5/55.2	1.83
1.0	76+23	259+52	11.8+1.5	81.9+5.9	68.0/60.3	1.35
1.0	75+22	435+49	63.4+1.9	49.8+1.3	82.9/69.4	2.42
1.0	65+15	229+42	85.3+2.0	45.6+1.2	80.5/71.3	3.43
1.0	53+18	275+30	143.6+.5	39.6+1.0	80.3/74.2	4.22
1.0	53+16	115+32	218.5+1	35.95+.95	80.3/74.3	4.91

Table 3
Selected Cusp-Trapped Electron Timescales.

Energy MeV	Gyration τ_1 ms	Bounce τ_2 ms	Drift τ_3 sec	μ keV/nT	CEqPA Deg	Cshell Re
1.2	50+15	580+68	26.0+4.3	55.7+5.0	42.4/49.8	1.26
1.2	50+14	557+86	50.0+1.4	53.0+1.7	51.5/55.2	1.83
1.2	245+75	381+56	22.0+1.2	78.6+1.4	81.2/70.9	2.00
1.2	105+36	222+43	53.6+1.6	59.81+.69	82.9/72.1	2.42
1.2	136+25	536+95	73.4+1.8	54.1+1.4	80.5/70.7	3.43
1.2	128+39	644+110	123.5+1.2	47.13+.82	80.3/73.9	4.22
1.2	105+38	406+54	187.5+1.2	42.93+.75	80.4/74.0	4.91
1.4	82+22	599+68	44.6+1.7	60.8+2.2	51.5/54.2	1.83
1.4	95+25	321+36	19.0+1.5	92.8+2.7	81.2/69.1	2.00
1.4	91+24	280+45	48.0+2.1	69.6+2.2	82.9/66.9	2.42
1.4	86+22	306+48	63.0+1.4	64.+1.1	80.5/74.2	3.43
1.4	47+12	586+32	105.4+2.0	55.5+1.0	80.3/74.1	4.22
1.4	48+13	630+230	165.	50.13+.96	80.4/73.6	4.91
1.6	93+32	560+100	39.6+2.1	71.0+3.1	51.5/55.1	1.83
1.6	204+85	323+75	18.0+1.4	102.5+6.4	81.2/62.1	2.00
1.6	184+80	416+63	41.2+1.0	79.7+2.0	82.9/71.8	2.42
1.6	327+66	368+37	57.3+1.7	71.9+2.2	80.5/68.9	3.43
1.6	215+53	653+49	99.8+1.1	62.1+1.6	79.6/72.0	4.13
1.6	357+40	831+62	147.33+.83	57.2+1.6	79.7/72.6	4.82
2.0	151+50	725+130	45.7+2.0	79.5+5.0	52.1/52.2	2.03
2.0	122+42	646+84	62.9+1.7	79.8+3.1	60.0/60.8	2.53
2.0	126+43	304+70	65.0+1.6	81.9+2.4	75.8/67.6	2.97
2.0	171+52	319+77	86.3+1.8	77.1+1.7	83.5/72.6	3.28
2.0	177+27	347+48	119.90+.91	71.45+.58	90.0/76.5	3.41
2.0	154+37	310+31	176.31+.79	67.00+.47	84.2/77.7	3.56
3.0	280+178	607+114	28.1+2.0	133.+15.	52.1/53.7	2.03
3.0	295+96	815+360	47.8+2.0	114.7+9.4	60.0/57.2	2.83
3.0	244+67	532+190	41.9+1.7	126.1+3.6	75.9/65.1	2.97
3.0	289+92	563+131	60.0+2.1	115.5+2.5	83.5/68.5	3.28
3.0	191+36	398+87	119.7+.70	107.2+.88	90.0/76.5	3.41
3.0	279+61	579+106	123.1+1.1	100.10+.79	84.2/76.0	3.56
4.0	468+139	832+294	48.0+1.1	149.6+7.5	65.7/58.1	2.97
4.0	525+174	814+162	52.8+1.0	148.1+6.8	78.1/62.5	3.28
4.0	456+128	894+191	64.0+2.1	143.4+3.6	90.0/68.7	3.40
4.0	375+112	875+124	95.7+1.4	133.3+1.8	84.1/73.5	3.56
6.0	499+144	1105+277	53.0+2.3	206.5+5.0	71.6/62.8	4.61
6.0	644+227	1324+251	65.8+1.4	198.7+2.0	84.1/72.4	3.56

Table 4
Relative Flux Increase for Fast Over Slow Wind

E/kT α	1.5	3	6	12	24	48	72
5.00	-0.856	-0.751	-.143	11.3	3.19e3	2.67e8	2.14e13
4.00	-0.802	-0.660	0.151	14.8	3.70e3	2.45e8	1.53e13
3.00	-0.704	-0.499	0.623	19.1	3.66e3	1.41e8	5.01e12
2.00	-0.489	-0.189	1.253	18.5	1.64e3	1.25e7	8.59e10
1.50	-0.280	0.027	1.228	10.3	3.04e2	2.31e5	1.55e08
1.25	-0.138	0.091	0.815	4.22	4.35e1	3.26e3	2.13e05
1.10	-0.050	0.066	0.366	1.28	5.40e0	4.97e1	3.65e02

Table 5
Storm Hardness Ratios

Year.DOY	>1.5 MeV rad/day	>3.5 MeV rad/day	h
1996.090	2.3	55	4
1996.120	5	110	5
1996.270	4	80	5
1997.010	2	50	3
1998.130	2	80	2.5
1998.240	12	200	6
1999.050	2	60	3
1999.250	3	70	4
1999.290	3	60	5